Applying a Random Time Mapping to Mann modelled turbulence for the generation of intermittent wind fields

Khaled Yassin[1], Arne Helms[2], Daniela Moreno[1], Hassan Kassem[3], Leo Höning[2,3], and Laura J. Lukassen[1]

[1]ForWind, Institute of Physics, Carl von Ossietzky University Oldenburg, Küpkersweg 70, 26129 Oldenburg, Germany
[2]Institute of Physics, University of Oldenburg, Carl von Ossietzky University Oldenburg, Küpkersweg 70, 26129 Oldenburg, Germany
[3]Fraunhofer Institute for Wind Energy Systems – Fraunhofer IWES, Küpkersweg 70, 26129 Oldenburg, Germany

Correspondence: Khaled Yassin (khaled.yassin@uni-oldenburg.de), Laura J. Lukassen (laura.lukassen@uni-oldenburg.de)

Abstract. A new approach to derive a synthetic wind field model which combines spatial correlations from the Mann model and intermittency is introduced. The term intermittency describes the transition from Gaussian to non-Gaussian velocity increment statistics at small scales, where non-Gaussian velocity increment statistics imply a higher probability for extreme values than a Gaussian distribution. The presented new model is named the Time-mapped Mann model. The intermittency is introduced
5 by applying a special random time-mapping procedure to the regular Mann model. The Time-mapping procedure is based on the so-called Continuous-time random walk model. As will be shown, the new Time-mapped Mann field reflects spatial correlations from the Mann model in the plane perpendicular to flow direction and temporal intermittency. In a first wind turbine study, the new Time-mapped Mann field and a regular Mann field are used as inflow to a wind turbine in a Blade Element Momentum simulation. It is shown that the wind field intermittency carries over to the loads of the wind turbine, and,
10 thus, shows the importance of carefully modeling synthetic wind fields.

1 Introduction

Wind energy plays a leading role in the energy transition process to renewable energy these days. In 2020, the world witnessed new wind energy installations by 93 GW to make the global installed capacity of wind energy 743 GW according to the Global
15 Wind Energy Council (GWEC (2021)). The growing demand on wind energy resulted in growing turbine rotor diameters. This leads to an increase of loads on the different turbine components like blades and tower. Numerical simulations are now crucial to predict loads and performance parameters in the early design stages. In this context, wind fields should be accurately simulated to be able to anticipate extreme load cases and fatigue loads on different parts of the wind turbine to reach the optimum design without compromising the structural limits of theses components. However, the physics of the turbulent wind fields are
20 not yet completely understood and many models were proposed to simulate these fields as described in the following.

The IEC 61400-1 standard for wind turbines (Han (2007)) recommends using Gaussian based atmospheric turbulence models, namely Kaimal (Kaimal et al. (1972)) and Mann (Mann (1994, 1998)) models to simulate turbulent wind fields. These two turbulent wind field models imply the assumption that the velocity increments of the wind fields behave in a Gaussian manner. However, it is well documented that the velocity increments of real atmospheric wind fields show non-Gaussian behavior, which is widely called intermittency. Through the heavy tails of the distribution this implies a larger probability for extreme values than in a Gaussian distribution. Boettcher et al. (2003) showed that wind field measurements from near the German North Sea cost line have a non-Gaussian distribution of two-point statistics of velocity increments for certain mean wind velocity intervals. Also, Vindel et al. (2008) have shown the intermittency of velocity increment statistics in data of the atmospheric boundary layer velocity measured by Cuxart et al. (2000). More recent researches like the work of Liu et al. (2010) and Mücke et al. (2011) reached the same conclusion. This means that extreme wind velocity increments happen more often than what is predicted using the turbulence models recommended by the IEC standard. Also, Morales et al. (2012) presented a statistical scheme to assess turbulent wind fields that uses both, lower and higher order one-point and two-point statistics. They have also compared synthetic turbulent time series using the Kaimal model with atmospheric turbulent wind field measurements from the research platform FINO-1. They have shown that the synthetic fields generated with the Kaimal model failed to grasp the intermittent behavior of the wind field.

The questions that arise at this point are, how a synthetic wind field can be modeled as realistic as possible and how this is reflected on the turbine loads. In this direction, Kleinhans (2008) proposed a new approach to generate an intermittent wind field using the Continuous Time Random Walk (CTRW) theory. This approach is based on stochastic differential equations and function that maps from an intrinsic time to real time to generate such an intermittent field whereas the spatial correlations are not as realistic as in the Mann field. A brief description of the CTRW model will be introduced in Sec. 2.3. In addition to the CTRW model, there also exist other models which can be applied to to generate synthetic wind fields with intermittent features, e.g. by Friedrich et al. (2021) based on multi-point statistics which are not further discussed here.

Gontier et al. (2007) compared the effect of the intermittent CTRW wind field and other standard turbulence models (Kaimal and von Kármán (1948)) on the fatigue loads of the D8 small wind turbine at different wind speeds. The authors have found that the simulated wind turbine loads in case of using the CTRW wind model is different from the loads simulated by using the other two models. However, the authors could not give definitive conclusions regarding the peak loads from their simulations. Later, Mücke et al. (2011) compared the statistics of wind fields generated by the Kaimal model, intermittent wind fields generated using CTRW and the atmospheric wind data measured within the GROWIAN project (Körber et al. (1988)). The three cases were then used in the NREL FAST (V6.01) (Jonkman and Jonkman (2005)) Blade Element momentum (BEM) simulator to model the resulting rotor torque of the 1.5MW WindPACT (Malcolm and Hansen (2006)) turbine. Also, the authors analyzed the stress cycles for the rotor torque time series to study the effects of the three wind fields on fatigue loads. They have concluded that the statistics of the numerical results using the Kaimal wind field qualitatively differ from the results obtained from measurements. On the other hand, they have concluded that CTRW simulated wind statistics agree quite well and also provided the intermittent rotor torque statistics very close to the resulting torque from measurements.

Gong and Chen (2014) numerically investigated the short- and long-term extreme responses of the onshore NREL 5MW tur-

bine for a Gaussian wind field using a Kaimal wind spectrum and a second non-Gaussian wind field generated by a translation process theory introduced by Gioffre et al. (2000). They showed that the non-Gaussian wind field resulted in larger extreme loads of the blade root edge-wise and tower for-aft moments while the responses of a stand-still wind turbine case were less sensitive to the non-Gaussanity of the wind field. Schottler et al. (2017) applied an intermittent wind field on a 0.58m diameter

60 model wind turbine in a wind tunnel to measure the effect of such a wind field on the thrust, power and torque on the rotor. The authors found out that the turbine did not smooth out the intermittency and they also concluded that assuming non-Gaussian wind fields may lead to significant differences in loads on the turbine.

Schwarz et al. (2018, 2019) isolated and investigated the effect of intermittent wind velocity on equivalent fatigue loads of the NREL 5MW wind turbine at different wind speeds using BEM simulations. To isolate the effects of intermittency, two different

65 velocity fields were generated by means of the CTRW model: a Gaussian and a non-Gaussian wind field. Both of them have the same features except for the intermittency that was introduced in the non-Gaussian field by means of the time mapping, which was simply omitted in the Gaussian case. For the two wind cases, three different spatial correlations were investigated: fully correlated fields, delta-correlated fields, and 3×3 sub-divided fully correlated fields. After analyzing the results of the different cases, the authors noticed that the highest effect of intermittency of the wind fields on the loads can be observed in

70 the fully correlated case with 5% to 10% increase in fatigue loads while it completely disappears in the the delta-correlated field. For the 3×3 sub-divided fully correlated field, intermittent loads were ranged between the other two cases. The authors concluded that intermittency in the wind field had a significant effect on loads. Berg et al. (2016) also compared Gaussian and non-Gaussian wind fields using Large Eddy Simulations (LES) in the HAWC2 Computational Fluid Dynamics (CFD) software (Larsen and Hansen (2007)). They studied the effect of the intermittency on different blade, tower and shaft loads and deflec-

75 tions of the NREL 5MW wind turbine. In contrast with the aforementioned studies, they concluded that the intermittency has no significant effect on the studied parameters. This shows that even though many studies reveal the influence of intermittency, the effect needs further investigation.

In this paper, a novel method to numerically generate a synthetic, intermittent turbulent wind field is introduced. Within this new method, the time-mapping technique introduced by Kleinhans (2008) is applied on a turbulent wind field generated by

80 the Mann model. A detailed comparison between our new wind field using this time-mapping technique, referred to as Time-mapped Mann field in the following, and a standard Mann modeled wind field is carried out. As will be shown, the advantage of the new Time-mapped Mann field is that it combines spatial correlations from the Mann wind field and intermittent behavior. Also, a first insightful comparison between selected mechanical loads on a 1.5MW wind turbine resulting from both Time-mapped Mann field and the standard Mann field is illustrated. The analysis of these turbine loads reveals the effect of

85 intermittency on wind turbine loads.

2 Scientific background on synthetic wind fields

Before illustrating the derivation of the new Time-mapped Mann field, general wind field statistics that will be used to analyze the generated wind fields are introduced in Sec. 2.1. After that, in 2.2 and 2.3 the Mann and CTRW turbulent wind field models are introduced.

2.1 Statistics of wind fields

For any turbulent wind field, the wind velocity time series U_i can be expressed as a function of mean velocity $\langle U_i \rangle$ and velocity fluctuation u_i, with $i = 1, 2, 3$ in three-dimensional space:

$$U_i = \langle U_i \rangle + u_i, \tag{1}$$

where the angular brackets $\langle . \rangle$ denote an ensemble average. Throughout this paper, the ensemble average is partly replaced by spatial or temporal averages for practical purposes which will be indicated in the respective cases below. In our case, we assume only a mean velocity in x_1-direction, i.e. $\langle \boldsymbol{U} \rangle = (\langle U_1 \rangle, 0, 0)$ which is the inflow direction in the following. From this decomposition, the turbulence intensity (TI) can be calculated as follows:

$$TI_i = \frac{\sigma_i}{\langle U_1 \rangle} = \frac{\sqrt{\langle u_i^2 \rangle}}{\langle U_1 \rangle}, \tag{2}$$

where i indicates the direction in which the turbulence intensity is calculated with respect to the mean velocity in the inflow direction $\langle U_1 \rangle$, and σ_i as the variance of u_i. The turbulence intensity is a one-point statistics in space and time of wind fields. However, for information on the spatial structures, one-point statistics are not sufficient and two-point statistics should be used for more information about the wind fields. As an example, the co-variance tensor contains two-point statistics:

$$R_{ij}(\mathbf{r}, \boldsymbol{x}, t) = \langle u_i(\boldsymbol{x}, t) u_j(\boldsymbol{x} + \mathbf{r}, t) \rangle \tag{3}$$

where R_{ij} is the two-point correlation which is independent from the position $\boldsymbol{x}$ in case of homogeneous turbulence. Accordingly, the spectral velocity tensor for homogeneous turbulence resulting from a Fourier transform of Eq. (3) gives (Pope (2001)):

$$\Phi_{ij}(\boldsymbol{\kappa}, t) = \frac{1}{(2\pi)^3} \int\limits_{-\infty}^{\infty} \int\limits_{-\infty}^{\infty} \int\limits_{-\infty}^{\infty} R_{ij}(\mathbf{r}, t) \exp(-\mathrm{i}\boldsymbol{\kappa} \cdot \mathbf{r}) \mathrm{d}\mathbf{r}. \tag{4}$$

In this equation, $\boldsymbol{\kappa} = (\kappa_1, \kappa_2, \kappa_3)$ represents a three-dimensional wavenumber vector for the three directions. The one-dimensional spectrum is following from Eq. (4) by integration:

$$F_i(\kappa_1, t) = \int\limits_{-\infty}^{\infty} \int\limits_{-\infty}^{\infty} \Phi_{ii}(\boldsymbol{\kappa}, t) \mathrm{d}\kappa_2 \mathrm{d}\kappa_3 = \frac{1}{2\pi} \int\limits_{-\infty}^{\infty} R_{ii}(r_1, 0, 0, t) \exp(-\mathrm{i}\kappa_1 r_1) \mathrm{d}r_1 \tag{5}$$

where the double index does not indicate a summation here. The one-dimensional spectra with respect to κ_2 and κ_3 are computed accordingly. The spectral coherence for the wavenumber κ_1 with respect to two separate points in the $x_2 - x_3$ plane

reads (Mann (1994)):

$$coh_{ij}(\kappa_1, \Delta x_2, \Delta x_3, t) \equiv \frac{|\chi_{ij}(\kappa_1, \Delta x_2, \Delta x_3, t)|^2}{F_i(\kappa_1, t) F_j(\kappa_1, t)} \tag{6}$$

with $F_i(\kappa_1, t)$ from equation (5) and the cross spectra χ_{ij} as defined below:

$$\chi_{ij}(\kappa_1, \Delta x_2, \Delta x_3, t) = \frac{1}{2\pi} \int_{-\infty}^{\infty} R_{ij}(r_1, \Delta x_2, \Delta x_3) \exp(-i\kappa_1 r_1) dr_1 \tag{7}$$

$$= \int_{-\infty}^{\infty} \int_{-\infty}^{\infty} \Phi_{ij}(\boldsymbol{\kappa}, t) \exp(i(\kappa_2 \Delta x_2 + \kappa_3 \Delta x_3)) d\kappa_2 d\kappa_3. \tag{8}$$

Another example for two-point statistics are the increment statistics in space described by:

$$\tilde{v}_i(\boldsymbol{x}, \Delta \boldsymbol{x}, t) = u_i(\boldsymbol{x} + \Delta \boldsymbol{x}, t) - u_i(\boldsymbol{x}, t) \tag{9}$$

where $\Delta \boldsymbol{x}$ indicates the spatial step in three-dimensional space. Instead of spatial increments, one can also consider temporal increments as

$$v_i(\boldsymbol{x}, t, \tau) = u_i(\boldsymbol{x}, t + \tau) - u_i(\boldsymbol{x}, t) \tag{10}$$

where τ indicates the time lag. The so-called kurtosis allows a quantification of the deviation of the intermittent increment probability density function (PDF) from a Gaussian distribution (here introduced for the temporal increments from Eq. (10)):

$$\text{Kurt}(v_i)(\boldsymbol{x}, t, \tau) = \frac{\langle v_i(\boldsymbol{x}, t, \tau)^4 \rangle}{\langle v_i(\boldsymbol{x}, t, \tau)^2 \rangle^2}. \tag{11}$$

For a Gaussian distribution, the kurtosis equals 3 by definition, while higher values give an indication of a heavy-tailed distribution in which extreme velocity increment values have a higher probability than predicted by a Gaussian distribution. We assume statistically stationary turbulence and, hence, omit the time t in the equations in the following.

Fig. 1 shows characteristics of temporal velocity increment statistics of atmospheric wind speed measurements. The data were collected at the site of a Nordex wind turbine with hub height of 125m, located in Northern Germany. Around 500 time series of 10 minutes length were considered for the analysis. These time series correspond to the horizontal magnitude (u_1, u_2) of the wind speed measured at the hub height with a sampling rate of 50Hz; the vertical component (u_3) was neglected here. The increments for the atmospheric measured data $v_{meas} = \sqrt{u_1^2(\mathbf{x}, t+\tau) + u_2^2(\mathbf{x}, t+\tau)} - \sqrt{u_1^2(\mathbf{x}, t) + u_2^2(\mathbf{x}, t)}$ were calculated similar to Eq. (10). Fig. 1(a) presents the PDFs of v_{meas} introduced above. For comparison, all the PDFs are normalized to standard deviation equal to 1 and the corresponding Gaussian distributions are shown by a solid line. As can be observed, the PDFs of v_{meas} clearly deviate from the respective Gaussian distributions. Specifically, the distributions of v_{meas} show heavy tails which represent the high probability of extreme events, which is higher than for the Gaussian PDFs. Furthermore, this deviation is increasing with decreasing time lag τ. This effect, which is called intermittency, is a well-known feature of real wind as Vindel et al. (2008), Liu et al. (2010), Mücke et al. (2011), and many others have found. Fig. 1(b) shows the calculated

kurtosis of the PDFs according to Eq. (11) of the atmospheric increments v_{meas} as function of τ. The values of Kurt(v_{meas}) higher than 3 reveal the intermittent behaviour of the atmospheric data over a wide range of τ. For large values of τ, the value of the kurtosis saturates at Kurt ≈ 5. This robust intermittency on large scales of atmospheric increments could be explained by Böttcher et al. (2007) as a result of mixing of isotropic turbulent subsets which do not belong to the inertial range anymore.
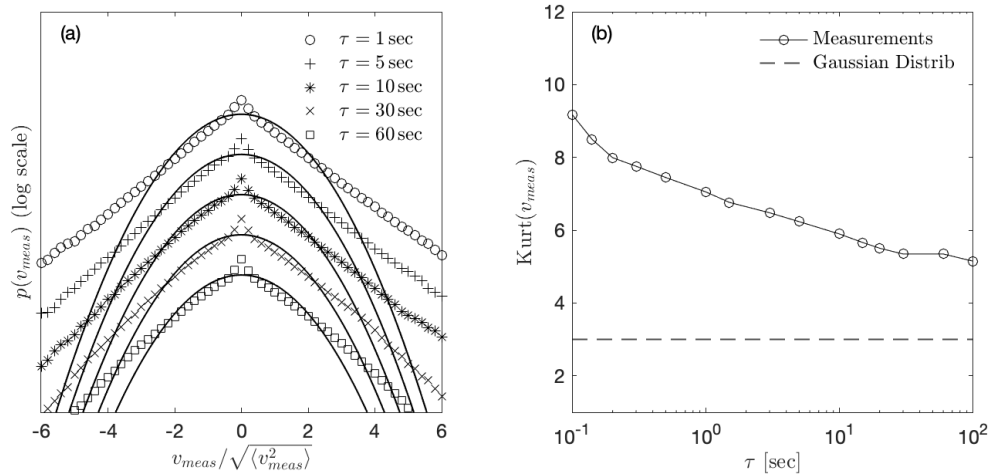
Figure 1. Statistical description of turbulent wind measurements from a Nordex wind turbine located in Northern Germany. (a) Normalized PDFs of velocity increments v_{meas} for different values of τ. The distributions for different values of τ, increasing from top to bottom, are depicted by different markers and are vertically shifted. (b) Kurtosis of velocity increments v_{meas} as function of τ. The angular brackets denote moving averages within the individual 600 s-time series and then over all data sets.

2.2 Mann Model

The basis of the Mann model (Mann (1994, 1998)) is a properly modeled spectral tensor according to Eq. (4). In this model, the turbulent velocity field is assumed to be incompressible and the velocity fluctuations are assumed to be homogeneous in space. The resulting velocity field depends on only three parameters, namely a length-scale L, a non-dimensional parameter Γ which is related to the eddy lifetime and, hence, to the shear gradient, and a parameter $c_K\epsilon^{2/3}$ with c_K as a constant and ϵ as the turbulent dissipation rate per unit mass. Within these assumptions, the second-order statistics such as variances and cross-spectra of real wind can be met. In case of isotropic turbulence (where assuming no shear) the spectral tensor takes the form Pope (2001):

$$\Phi_{ij}^{iso}(\boldsymbol{\kappa}) = \frac{E(\kappa)}{4\pi\kappa^4}\left(\delta_{ij}\kappa^2 - \kappa_i\kappa_j\right) \tag{12}$$

with κ as the magnitude of $\boldsymbol{\kappa}$ and $E(\kappa)$ as the energy spectrum. $E(\kappa)$ can be expressed with $c_K\epsilon^{2/3}$ and L that leads to (von Kármán (1948), Pope (2001)):

$$\Phi_{ij}^{iso}(\boldsymbol{\kappa}) = \frac{c_K\epsilon^{2/3}L^{17/3}}{4\pi}\frac{\delta_{ij}\kappa - \kappa_i\kappa_j}{[1 + (L\kappa)^2]^{17/6}}. \tag{13}$$

The corresponding one-dimensional spectra result in (Mann (1994)):

$$F_i(\kappa_1) = \begin{cases} \frac{9}{55}c_K\varepsilon^{2/3}\frac{1}{(L^{-2}+\kappa_1^2)^{5/6}} & \text{for } i = 1 \\ \frac{3}{110}c_K\varepsilon^{2/3}\frac{3L^{-2}+8\kappa_1^2}{(L^{-2}+\kappa_1^2)^{11/6}} & \text{for } i \in \{2,3\}, \end{cases} \tag{14}$$

accordingly, the variance becomes:

$$160 \quad \sigma_{iso}^2 = \sigma_1^2 = \sigma_2^2 = \sigma_3^2 = \frac{9}{55}\frac{\sqrt{\pi}\Gamma(\frac{1}{3})}{\Gamma(\frac{5}{6})}c_K\epsilon^{2/3}L^{2/3} \approx 0.688c_K\epsilon^{2/3}L^{2/3} \tag{15}$$

where in this equation the Γ denotes the mathematical Gamma function. The value of the $c_K\epsilon^{2/3}$ parameter can be found by fitting the model to specific site data assuming isotropic turbulence and an infinitely large domain. Another possible way to avoid such assumptions was suggested by Larsen and Hansen (2007) who suggest choosing the value of $c_K\epsilon^{2/3}$ arbitrarily and then re-scaling the velocity field with a scaling factor calculated by:

$$165 \quad SF = \sqrt{\frac{\sigma_{i,target}^2}{\sigma_i^2}} \tag{16}$$

where σ_i^2 is the variance of the original field and $\sigma_{i,target}^2 = TI_i^2\langle U_1\rangle^2$ as in Eq. (2) is the target variance of the field. In this work, the fields used in the simulations were not re-scaled. However, the value of $c_K\epsilon^{2/3}$ was taken according to the Engineering Sciences Data Unit (ESDU (1982)) spectral model to achieve $TI_1 \approx 10\%$ as will be explained later in details.

The Mann model provides a spatially correlated synthetic turbulent wind field where the spatial homogeneity is one of the
170 basic assumptions in deriving this model. However, since this model is based on the spectra but not on increment statistics of the atmospheric wind fields, it fails to display intermittency which should have effects on different turbine loads as shown in different former researches, cf. Sec. 1.

2.3 Continuous time random walk (CTRW) model

Kleinhans (2008) introduced the idea of generating a synthetic velocity time series $\mathbf{u}(s)$, on an intrinsic time scale s, based on
175 a coupled Ornstein-Uhlenbeck process (Uhlenbeck and Ornstein (1930)) for $\mathbf{u}(s)$ and a reference wind speed $\mathbf{u_r}(s)$. Instead of a mean velocity, this reference wind speed $\mathbf{u_r}(s)$ is used in the modeling process which influences the whole velocity field (Kleinhans (2008)).

After generating the velocity time series $\mathbf{u}(s)$ for all grid points in a plane perpendicular to the flow velocity, a stochastic process is applied to map the field from the intrinsic time s to the physical time domain t. This mapping process is the crucial
180 feature of the model for generating intermittent characteristics in the wind field. The mapping process is defined as (Fogedby (1994)):

$$\frac{dt(s)}{ds} = \tau_\alpha(s) \tag{17}$$

where τ_α follows an α-stable Lévy distribution with characteristic exponent α (Kleinhans and Friedrich (2007)):

$$(\tau_\alpha) = \frac{1}{\pi}\text{Re}\left\{\int_0^\infty dz\exp\left[-iz\tau_\alpha - z^\alpha\exp\left(-i\frac{\pi\alpha}{2}\right)\right]\right\}. \tag{18}$$

185 Kleinhans (2008) generated the random variable τ_α according to the implementation introduced by Weron (2001):

$$\tau_\alpha = \frac{\sin(\alpha(V + \frac{\pi}{2}))}{\cos(V)^{\frac{1}{\alpha}}} \left(\frac{\cos(V - \alpha(V + \frac{\pi}{2}))}{W} \right)^{\frac{1-\alpha}{\alpha}} \tag{19}$$

where V is a uniformly distributed random variable that takes a value in the range between $]-\frac{\pi}{2}, \frac{\pi}{2}[$ and W is an exponentially distributed variable with a mean value = 1. The Lévy distribution is truncated for $0 < \tau_\alpha < c$ if $0 < \alpha < 1$, where c is a cutoff. Kleinhans (2008) showed that when continuous stable Lévy processes are used for the transformation from the intrinsic time

190 (s) to the physical time (t), the process is dominated by "waiting" regions. In this context, these regions are periods during which the wind speed is constant, a feature that is not observed in the atmospheric wind. In order to limit those periods to a realistic length, the Lévy distribution is truncated at the cutoff c. When $\alpha = 1$, $p(\tau_\alpha)$ is not a Lévy distribution anymore. It becomes a δ-correlated distribution with $\tau_1 = 1$. In that case, the mapping process from s to t is linear which makes $\mathbf{u}(s) = \mathbf{u}(t)$ and no intermittent behavior is introduced to the field.

195 As mentioned before, the main advantage of the CTRW model is that it manages to generate an intermittent wind field. However, the original CTRW model proposed by Kleinhans (2008) assumes that the spatial correlations of the velocity fluctuations between different points of the grid decay exponentially with the distance between them. This assumption must be understood as a simplification of the atmospheric turbulence. A modified version of the original CTRW model was implemented by Schwarz et al. (2019) as introduced in Sec. 1. They generated individual CTRW time series and arranged them to generate

200 three different spatial correlations in the wind field. Firstly, they set up fully correlated wind fields by repeating the same velocity time series in the whole x_2-x_3 plane (perpendicular to the inflow direction). For the second arrangement, they generated delta-correlated wind fields by setting up an independent Ornstein-Uhlenbeck process in each point of the grid in the x_2-x_3 plane. Finally, they considered an intermediate version of a 3×3 sub-divided fully correlated wind field. In this third scenario, the rotor plane was divided in a 3×3 grid in which each cell corresponds to a fully correlated area, but the nine areas are

205 uncorrelated between them. They found different effects of the wind fields on the turbine loads depending on the resolution (i.e. fully correlated, delta-correlated or partially correlated). However, no conclusive recommendation was provided on which resolution is most realistic.

3 The new Time-mapped Mann model

The new proposed Time-mapped Mann model aims at maintaining the spatial correlation provided by the Mann model ex-

210 plained in Sec. 2.2 while introducing the intermittency by means of the time-mapping process of the CTRW model explained in Sec. 2.3. Accordingly, in our new Time-mapped Mann model, the Ornstein-Uhlenbeck process used to generate the wind field in the original CTRW model is replaced with a Gaussian wind field using Mann's model. The longitudinal spatial dimension in the Mann model is converted into the intrinsic time according to the Taylor hypothesis (Taylor (1938)). After that, the time mapping from intrinsic time s to physical time t is applied to each step n using the discretized form of Eq. (17) (Kleinhans

215 (2008)):

$$t(s_{n+1}) = t(s_n) + C_{\alpha,c,\Delta s_t} \tau_\alpha(s_n) \tag{20}$$

where $C_{\alpha,c,\Delta s_t}$ is a normalization factor that has the dimension of a time and depends on the Lévy exponent α, the cutoff c and the discretization parameter $\Delta s_t = s_{n+1} - s_n$. The intrinsic time step Δs_t is equidistant while the physical time step Δt_n is non-equidistant. The factor $C_{\alpha,c,\Delta s_t}$ is introduced so that the mean slope of $t(s)$ is one, which means that the development

220   of the physical time and the intrinsic time occurs statistically at the same speed.

As shown in Fig. 2, the Time-mapped Mann model generates a turbulent wind field which is spatially correlated in the two transversal directions (x_2 and x_3) since it is not changed from the original Mann model besides an interpolation procedure explained below. On the other hand, the conversion between the intrinsic and physical time scales using the random τ_α leads to intermittent behaviour in the longitudinal direction x_1 (or in other words in the temporal behavior since the longitudinal

225   direction x_1 is converted to time with Taylor's hypothesis), as will be shown in Sec. 4. Accordingly, it presents a compromise between Gaussian, non-intermittent fields generated using Mann model and the intermittent CTRW model.

(a) (b)
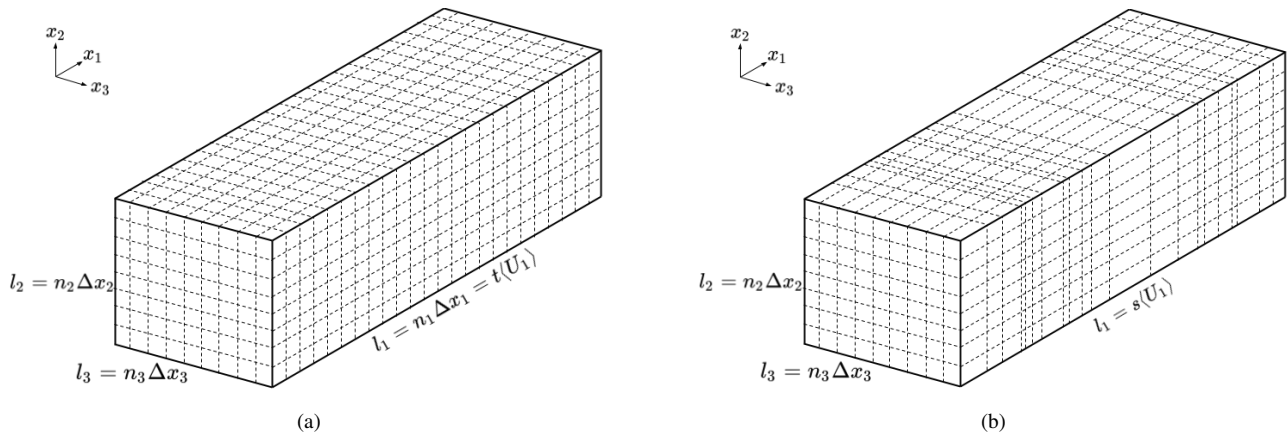
Figure 2. Schematic illustration of turbulence boxes generated by the (a) Mann model with equidistant steps and (b) Time-mapped Mann model after applying the time mapping process resulting in non-equidistant steps.

The effect of the generated intermittent wind field on the loads of a wind turbine is analyzed by means of a numerical BEM simulation (described in Sec. 4.2). This numerical model requires that the size of the time step Δt of the incoming wind field is equidistant during the simulation. However, as schematically shown in Fig. 2, the time mapping process described by Eq. (20)

230   generates non-equidistant time steps Δt_n, proportional to τ_α calculated with Eq. (19). Therefore, the wind speed U_i has to be linearly interpolated between the discrete points obtained with the random numbers τ_α to the required discrete points distanced by a fixed time increment Δt_{BEM}. An example of this interpolation is graphically illustrated in Fig. 3. The dashed vertical red lines correspond to the discrete times from the mapping process separated by $\Delta t_n \propto \tau_\alpha$. The red dots show the process U_i at those discrete times. Similarly, the continuous vertical black lines depict the times equally distanced by $\Delta t = \Delta t_{BEM}$.

235   Then, the linear interpolation takes place between the red dots to obtain the values of U_i at the times depicted by the black lines. The resulting equally distanced discrete points are shown by the black squares. For clarification purposes, the schematic illustrations shown in Fig. 2 and Fig. 3 do not correspond to the same time-mapping process but should just demonstrate the

mathematical process.

To generate a Mann box, the HAWC2 Mann turbulence generator tool (Larsen and Hansen (2007)) is used. After that, an
240   in-house Matlab (MATLAB (2019)) code is used to create the Lévy distribution for τ_α to apply the Time-mapping and inter-polation processes.
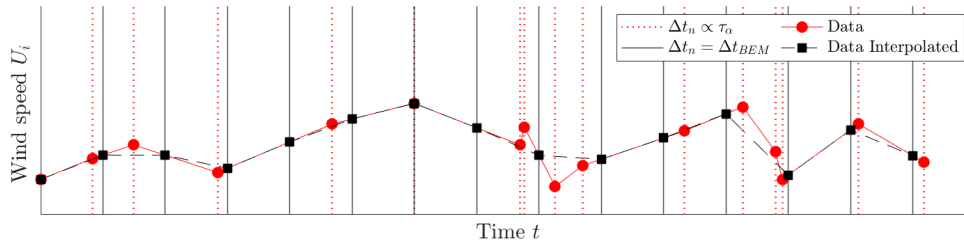
Figure 3. Schematic illustration of the interpolation from non-equally distributed time increments $\Delta t_n \propto \tau_\alpha$ to equally distributed time increments Δt_{BEM} for the BEM simulations.

4   Results and Discussion

In this section, the analysis of the new Time-mapped Mann wind field and exemplary resulting loads from this time mapping will be shown. To clarify the impact of intermittency on the wind fields and loads in this work, all cases will be compared to
245   the original Mann wind field generated with the same parameters to provide a fair comparison between the two models.

4.1   Characteristics of the Time-mapped Mann model

This section provides a thorough comparison of statistical quantities such as the spectral tensors, the coherence, and the velocity increment distribution of both fields, the regular Mann and the new Time-mapped Mann wind field. The dimensions of the grid for the generation of the wind fields are selected according to Table 1, such that they can be used for the BEM simulations in
250   Sec. 4.2. In this case, the defined grid has 32×32 nodes with $\Delta x_2 = \Delta x_3 = 2.6m$ covering a $80.6m \times 80.6m$ area. The original Mann field is generated using the Mann model at mean wind speed $\langle U_1 \rangle = 20\ ms^{-1}$, turbulence intensity in the flow direction (which is x_1 direction in this case), $TI_1 = 10\%$, $\Gamma = 0$, and $c_K \epsilon^{2/3} = 0.62\ m^{4/3}s^{-2}$ according to the parameters of the Mann model as introduced in the ESDU spectral model. Corresponding to $\Gamma = 0$, we assume homogeneous turbulence, and wind shear is not taken into consideration in this work. Also, based on this assumption, the velocity components can be averaged
255   over each slice to calculate the wind field statistics. According to Kelly (2018), the L parameter can be calculated by:

$$L = z \frac{TI_1}{a} \tag{21}$$

where z is the height of the calculation point (which is the turbine hub height in this work) and a is a shear exponent. Even though, we assume no shear in this work, the shear exponent value a is only used to calculate the value of L with no effect on

the wind velocities. According to the hub height of the studied 1.5MW turbine with $z = 84m$, and for neutral conditions with

260   a shear exponent of $a = 1/7$ (Schlichting and Gersten (2016)), Eq. (21) results in $L = 58.8m$.

Table 1. Mann box and time-mapping parameters for the generated wind fields.

n_{x_1}	$n_{x_2} = n_{x_3}$	Δx_1	$\Delta x_2 = \Delta x_3$	Γ	L	$c_K \epsilon^{2/3}$	TI_1	$\langle U_1 \rangle$	α
$[-]$	$[-]$	$[m]$	$[m]$	$[-]$	$[m]$	$[m^{4/3}s^{-2}]$	$[\%]$	$[ms^{-1}]$	$[-]$
1.31072×10^5	32	2	2.6	0	58.8	0.62	10	20	0.6

For the Time-mapped Mann wind field, the three components of the velocity fluctuations of each transverse plane (x_2-x_3 in this case) are shifted according to the resulting $t(s)$. When applying the time mapping process to the wind field, the same stochastic process ($C_{\alpha,c,\Delta s_t}\tau_\alpha(s_n)$) is applied to each point of the x_2-x_3-plane and it is not a function of the location of different points in the x_2-x_3-plane. Fig. 4 shows the resulting relationship between intrinsic time scale (s) and real time scale

265   (t) used in the time mapping process of the original Mann field to the new Time-mapped Mann field according to Eq. (20) for different values of α (in the Lévy distribution). As noticed from this figure, the relationship between s and t is not an exact straight line, which means that the resulting field will be different from the original field as explained in Sec. 3. The values of τ_α in Eq. (20) follow a Lévy's distribution with the corresponding PDFs presented in Fig. 5 at different values of α. In the following analysis and simulations, we will only consider $\alpha = 0.6$, which is highlighted with red lines in Fig. 4 and 5.

270   Additionally, values of c=20 and Δs_t=8 sec were considered for the calculation of the scaling factor $C_{\alpha,c,\Delta s_t}$ in Eq. (20).
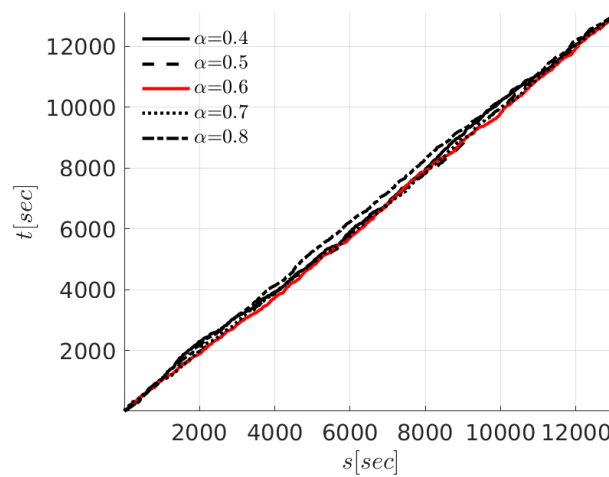
Figure 4. Relationship between intrinsic time scale (s) to physical time scale (t) (resulted from τ_α in Eq. (20)) at different values of α.
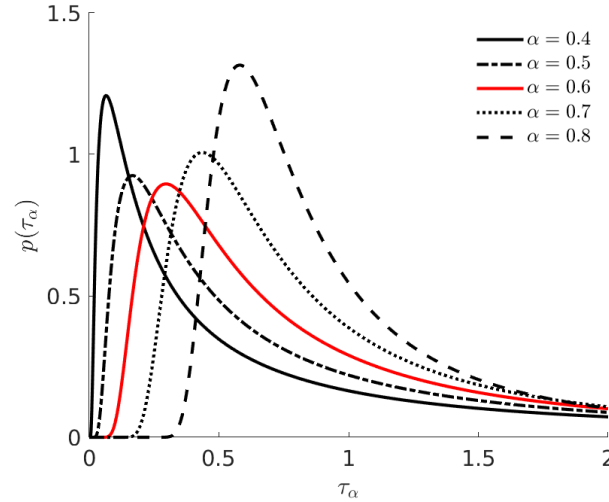
Figure 5. Lévy probability distribution of τ_α as in Eq. (18) at different values of α.

The comparison between the Mann and the new Time-mapped Mann wind fields regarding statistical properties is performed in terms of one-point and two-point statistics from Sec. 2.1. Starting with one-point statistics, the values of the mean wind speed in the longitudinal direction U_1 and the corresponding standard deviation $\sqrt{\langle u_1^2 \rangle}$ are presented in Table 2. These values are calculated from the time series at the hub-point (location of the hub of the turbine in the BEM simulations, see Sec. 4.2). For

275 better comparison, the relative differences (Rel.Diff) calculated as the difference between both results over the result from Mann field (i.e. (Time-map. − Mann)/Mann), are also presented in the table. The differences in the Time-mapped Mann model come from the interpolation procedure applied after the mapping process, illustrated in Fig. 3.

The values of the relative differences for $\langle U_1 \rangle$ and $\sqrt{\langle u_1^2 \rangle}$ are lower than 2%. This means, in terms of one-point statistics at hub-

Table 2. Values of the mean wind speed and standard deviation at the hub-point in the longitudinal direction ($\langle U_1 \rangle$ and $\sqrt{\langle u_1^2 \rangle}$) for the Mann (Mann) and Time-mapped Mann (Time-map) wind fields.

mean $\langle U_1 \rangle$ (hub)			standard deviation $\sqrt{\langle u_1^2 \rangle}$ (hub)		
Mann	**Time-map.**	**Rel.Diff**	**Mann**	**Time-map.**	**Rel.Diff**
$20.02\ ms^{-1}$	$19.98\ ms^{-1}$	-0.20%	$1.99\ ms^{-1}$	$1.96\ ms^{-1}$	-1.51%

point, the two generated wind fields are comparable. The slight differences between the two fields are caused by interpolation

280 procedure explained in Fig. 3. However, one-point statistics are not enough to show the effects of intermittency.

To show the effect of the time mapping on the spectral properties of the new field, Fig. 6 shows a comparison between the spectra $\langle F_i(\kappa_i) \rangle_{\mathcal{I}}$ of three components of the original Mann field and the new Time-mapped Mann field. In these figures, $\langle . \rangle_{\mathcal{I}}$ denotes spatial averaging over the plane $\mathcal{I} = \{(x_2, x_3) | 0 \leq x_2 \leq l_2, 0 \leq x_3 \leq l_3\}$. Fig. 6(a) shows the wavenumber spectrum

of the u_1-velocity component in the longitudinal (x_1) direction, while Fig. 6(b) and 6(c) show the same comparison but for

285   u_2 component in the x_2- and u_3 component in the x_3-directions, respectively. The theoretical spectra of the Mann field from Eq. (14) are plotted in the same figures to show how the spectra should be distributed over the different wavenumbers. Further to that, an uncorrelated, intermittent wind field was also added for the comparison. This uncorrelated wind field is generated by arbitrarily shuffling the grid points of the intermittent Time-mapped Mann field in the transverse directions (x_2 and x_3 directions). This uncorrelated field is generated to show the difference between a correlated field in the transverse directions

290   (which is the Time-mapped Mann field) and a completely uncorrelated turbulent field (in the transverse direction).

Fig. 6, shows that the Mann and Time-mapped Mann fields are behaving almost in the same manner. Discrepancies arise through the time-mapping procedure and the interpolation procedure that is needed as described in Sec. 3. Fig. 6(a) shows that both, the Time-mapped Mann field and the Mann field slightly differ in the lower and higher wavenumbers whereas both are still close to the theoretical curve. Fig. 6(b) and (c) show that both, the Mann and Time-mapped Mann have the same

295   behavior for low wavenumbers. The deviation between the two fields at high wavenumbers comes due to the interpolation illustrated in Sec. 3 and in this case due to the low number of grid points in the transverse directions ($n_{x_2} = n_{x_3} = 32$). A further investigation of these interpolation discrepancies is shown in the appendix A1 where the spectra of a wind field with an equal number of grid points in all directions $n_{x_1} = n_{x_2} = n_{x_3} = 512$ (cubic case) are shown. The spectra of these fields in Fig. A1 show that for a finer discretization in x_2 and x_3 directions, the discrepancies between the curves almost vanish whereas

300   the coarser discretization in the x_1-direction increases the discrepancy for the large wavenumbers. This shows the effect of the interpolation on the differences at high wavenumbers in Fig. 6.

For the uncorrelated intermittent field, we can see a good agreement between this field and the Time-mapped Mann field in the longitudinal direction x_1 since the arbitrary shuffling was only applied in the transverse directions. For the spectra in the transverse directions, the spectra are around unity regardless of the wavenumber, which proves the destruction of the correlation

305   in the transverse directions due to this shuffling.
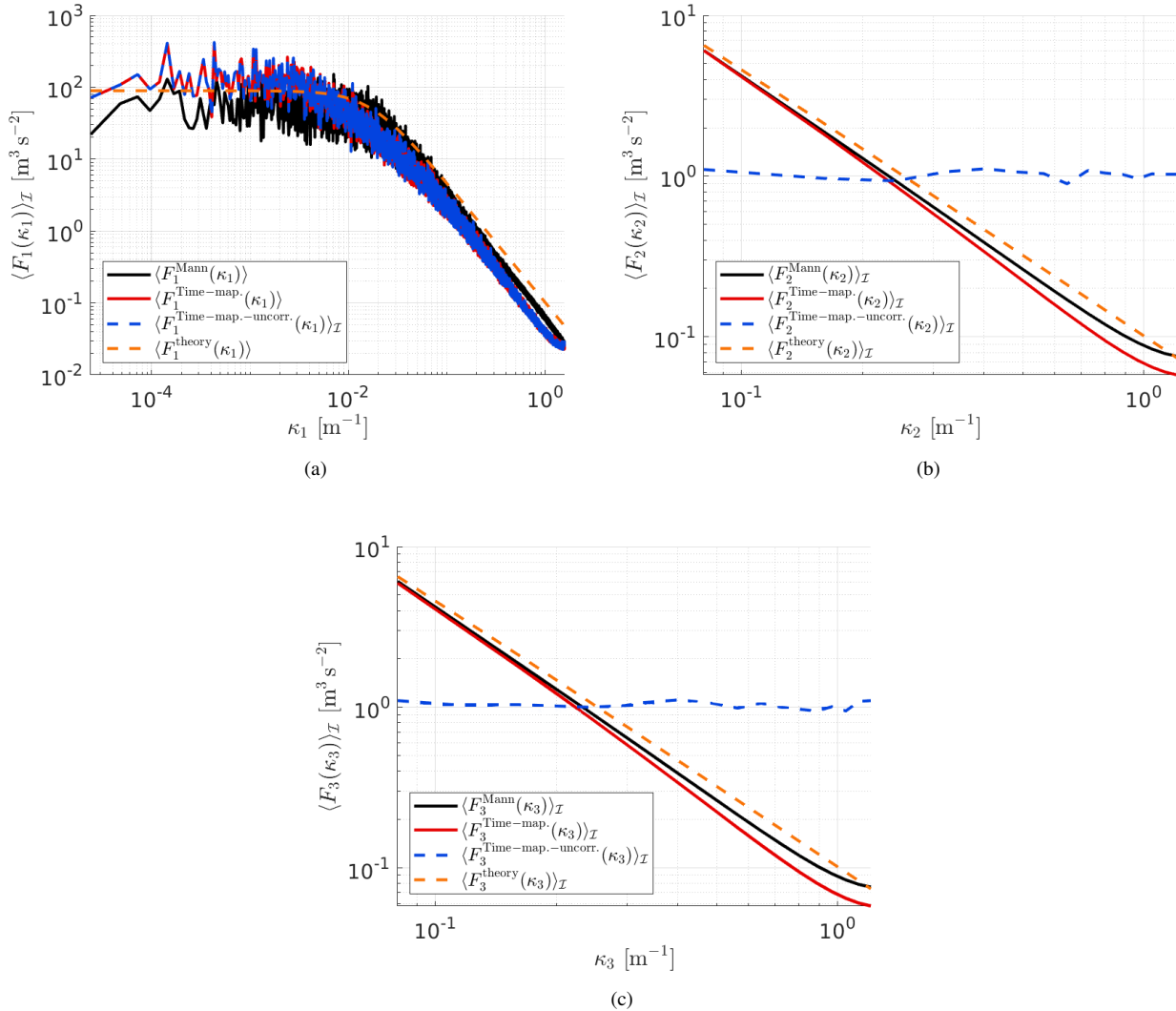
Figure 6. Comparison of averaged spectra in (a) x_1-, (b) x_2-, and (c) x_3-directions for the Mann field ($F_i^{\text{Mann}}(\kappa_i)$), the Time-mapped Mann field ($F_i^{\text{Time-map.}}(\kappa_i)$), an uncorrelated Time-mapped Mann field e.g.: ($F_i^{\text{Time-map.-uncorr.}}(\kappa_i)$) and the theoretical spectra ($F_i^{\text{theory}}(\kappa_i)$) calculated from Eq. (14)

To see the differences between the Mann and the Time-mapped Mann field more clearly than in the spectra, the coherence of velocity components (Eq. (6)) of the two wind fields in the three spatial directions is plotted versus $\kappa_1 \Delta x_2$ in Fig. 7. In this figure, the difference in coherence of the two fields as we move in x_2-direction are obvious due to the time mapping in the longitudinal direction. On the other hand, a comparison between the coherence of the two wind fields versus $\kappa_2 \Delta x_3$ for the
310 cubic case is shown in Fig. A2 in the appendix. In the latter case, the differences in coherence between the two fields are small. This is due to the unchanged x_2-x_3 planes during the time mapping process. This shows that the coherence with respect to the

longitudinal direction is highly influenced by the time mapping whereas it is not with respect to the transverse direction.

Following on from the two-point statistics analysis, the velocity increments v_1 defined in Eq. (10) and the degree of inter-
315 mittency of the wind fields are analyzed. Fig. 8 shows the comparison between the PDFs of the velocity increment of both, the Mann and the new Time-mapped Mann wind fields. It is obvious in this figure how extreme events in case of the Time-mapped wind field (the red markers) have a higher probability than the corresponding events in case of the Gaussian Mann field (the black markers). Also, it can be noticed that the intermittency increases with the decrease of τ. Note that this τ refers to the temporal increment in Eq. (10) and not to the τ_α introduced in the context of the Lévy distribution. Another important measure
320 of the increment statistics is the kurtosis calculated from Eq. (11). In the case of the kurtosis of the wind fields, the angular brackets denotes averaging over time and kurtosis in this case is only a function of τ Fig. 9 shows a comparison between the kurtosis of the velocity increment from the Mann field and the Time-mapped Mann fields at different τ values. As explained earlier, higher values of τ show a Gaussian distribution with kurtosis of 3 and lower values of τ show more deviation from the Gaussian PDF of the Mann field.
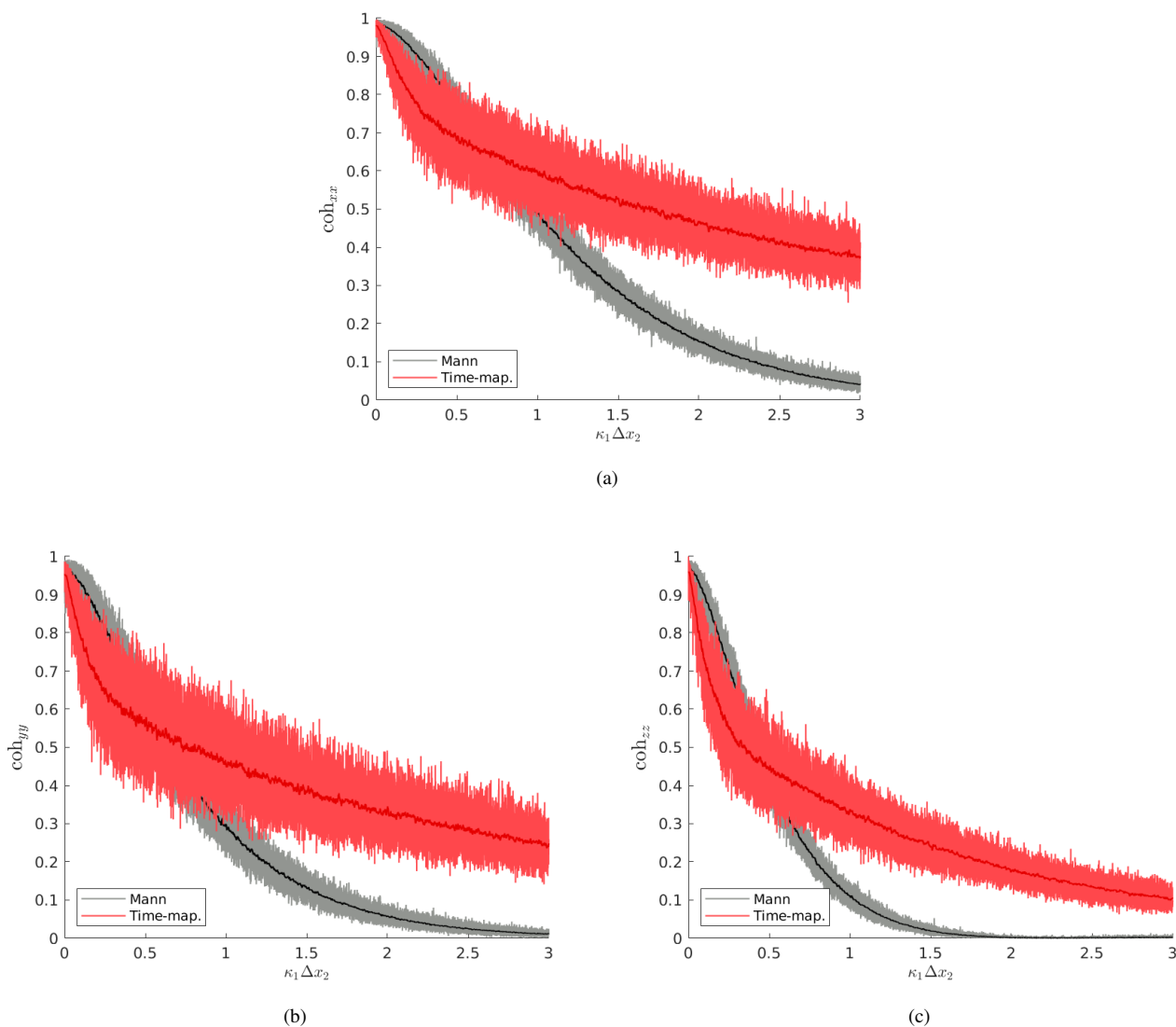
Figure 7. Comparison of the coherence of velocity components in (a) x_1-, (b) x_2-, and (c) x_3-directions for both Mann and Time-mapped Mann fields over wavenumber $\kappa_1 \Delta x_2$ with $\Delta x_2 = 2.6$ and $\Delta x_3 = 0$. Dark lines represent smoothed coherence values of the light lines using a moving average method.
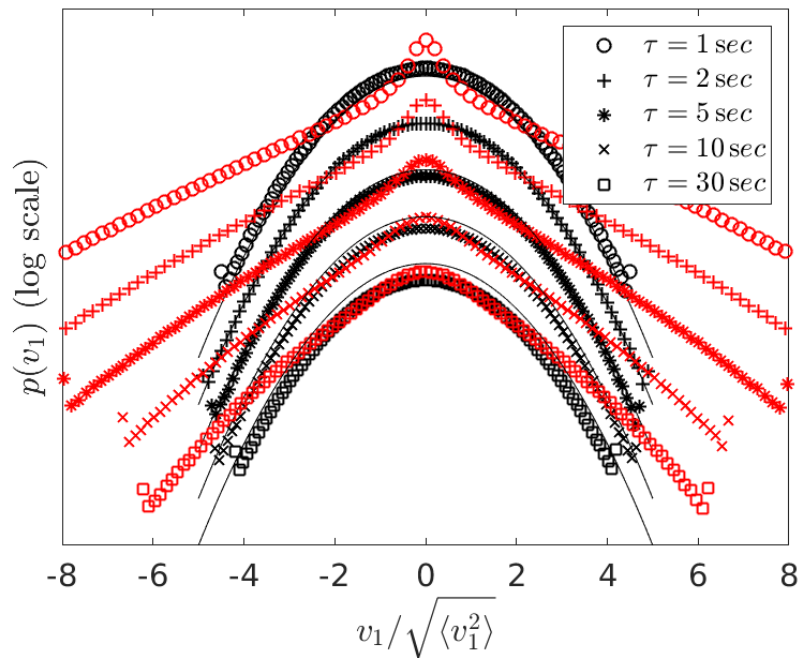
Figure 8. Spatially averaged PDF over transverse planes of velocity increments of the Mann wind field (black) and the Time-mapped Mann wind field (red) at different temporal increments τ. The black thin lines are Gaussian distributions as a reference. The curves are shifted vertically for visualization.
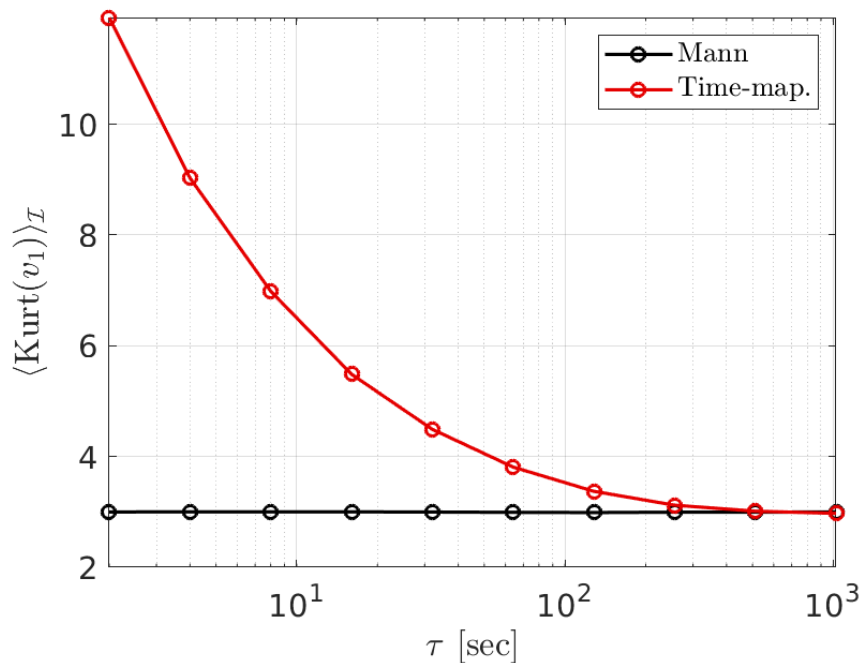
Figure 9. Kurtosis of Mann (black) and Time-mapped Mann (red) fields (Eq. (11)) at different temporal increments τ. For a Gaussian distribution the kurtosis is 3.

4.2 Analysis of the resulting wind turbine loads

After analyzing the effect of the time mapping on the different statistics of the wind fields in the previous section, here, the effect on exemplary turbine loads is studied. The main point of this section is to see whether the intermittency from the wind field is carried to the turbine structure. If the turbine loads are proved to reflect intermittency, this might have a significant effect on the dynamic loads acting on the wind turbine. For example, the damage equivalent loads (DEL) calculated from fatigue analysis might be affected due to intermittency because the probability for extreme values in the load increments is larger than for a Gaussian distribution.

In this work, BEM simulations of the NREL WindPACT 1.5MW (Malcolm and Hansen (2006)) virtual wind turbine are performed using the aero-elastic simulator NREL FAST (v8.16) (Jonkman and Jonkman (2016)). The main characteristics of the turbine and input parameters for the simulations are summarized in Table 3. The wind fields used in these simulations are the same Mann and Time-mapped Mann fields analyzed and compared in Sec. 4.1.

Parameter	Value/Description
Mean wind speed $\langle U_1 \rangle$	$20 \ ms^{-1}$
Mean wind speed $\langle U_2 \rangle$ and $\langle U_3 \rangle$ (averaged over transverse plane)	$0 \ ms^{-1}$
Turbulence Intensity $(TI_1 = TI_2 = TI_3)$ at hub (Eq. (2))	0.10
Wind shear	No
Rotor diameter	70 m
Hub height	84 m
Control	Fixed pitch - Fixed speed
Rotor speed	20 rpm
Pitch angle	20°
Simulation time	13100 s
Sampling frequency	20 Hz
Structural degrees of freedom (DOF)	Turned off
Tower passage	Turned off
Wake model	BEM Model

Table 3. Main parameters of the turbine and numerical simulations.

Four different load sensors were selected for analyzing the effect of the intermittent wind: the bending moment at the root of the blade in the flapwise direction (`RootFlap`), the rotor torque (`Torque`), the rotor thrust (`Thrust`) and the bending

340   moment at the base of the tower in the fore-aft direction (`TwrForeAft`). According to Schwarz (2020), these four sensors are expected to be highly sensitive and mainly dominated by aerodynamic forces in the direction of the flow and not by other sources of load such as gravitational forces.

Firstly, the mean values and standard deviations calculated over the length of the simulation are presented in Table 4. Here, the results for the four load sensors of both, the Time-mapped Mann (Time-map.) and the Mann (Mann) wind field are shown. Moreover, the relative differences (Rel.Diff) were also calculated (i.e. $(\text{Time-map.} - \text{Mann})/\text{Mann}$). In Table 4, the relative

Sensor/Load	Mean Value			Standard Deviation		
	Mann	**Time-map.**	**Rel.Diff**	**Mann**	**Time-map.**	**Rel.Diff**
RootFlap	861 kN.m	868 kN.m	0.81%	253 kN.m	251 kN.m	-0.79%
Torque	1126 kN.m	1136 kN.m	0.89%	269 kN.m	267 kN.m	-0.74%
Thrust	157.76 kN	158.77 kN	0.64%	24.16 kN	24.09 kN	-0.29%
TwrForeAft	10317 kN.m	10406 kN.m	0.86%	2017 kN.m	2017 kN.m	0%

Table 4. Mean values and standard deviations of time-series from BEM simulations for the Mann (Mann) and the Time-mapped Mann (Time-map.) wind fields. The relative differences (Rel.Diff.) between the two cases are calculated for better interpretation.

345

differences of the mean values and standard deviations of the analyzed sensors are less than $\pm 1\%$ between the Mann and the Time-mapped Mann wind field. It can be seen that this difference is in the same order as the differences in the mean wind speed $\langle U_1 \rangle$ and standard deviation $\sqrt{\langle u_1^2 \rangle}$ at the hub point presented in Table 2. In order to investigate whether the intermittency in the wind field carries over to the turbine loads, the incremental statistics of the loads are evaluated. The load increments M_τ

350 are defined similarly to velocity increments in Eq. (10):

$$M_\tau(t,\tau) = M(t+\tau) - M(t) \tag{22}$$

where M is the time series of the load sensor and τ corresponds to the time lag. Fig. 10 shows the PDFs of M_τ for the four selected load sensors, for $\tau = 1$s (top) up to $\tau = 30$s (bottom). For a direct comparison to the PDFs of the velocity increments

355 v_1, the values of τ are selected analogously to Fig. 8. Similar to Fig. 1 and 8, all the indivual PDFs are normalized to standard deviation $\sqrt{\langle M_\tau^2 \rangle} = 1$. Here, the angular brackets denote moving averages over the time series.
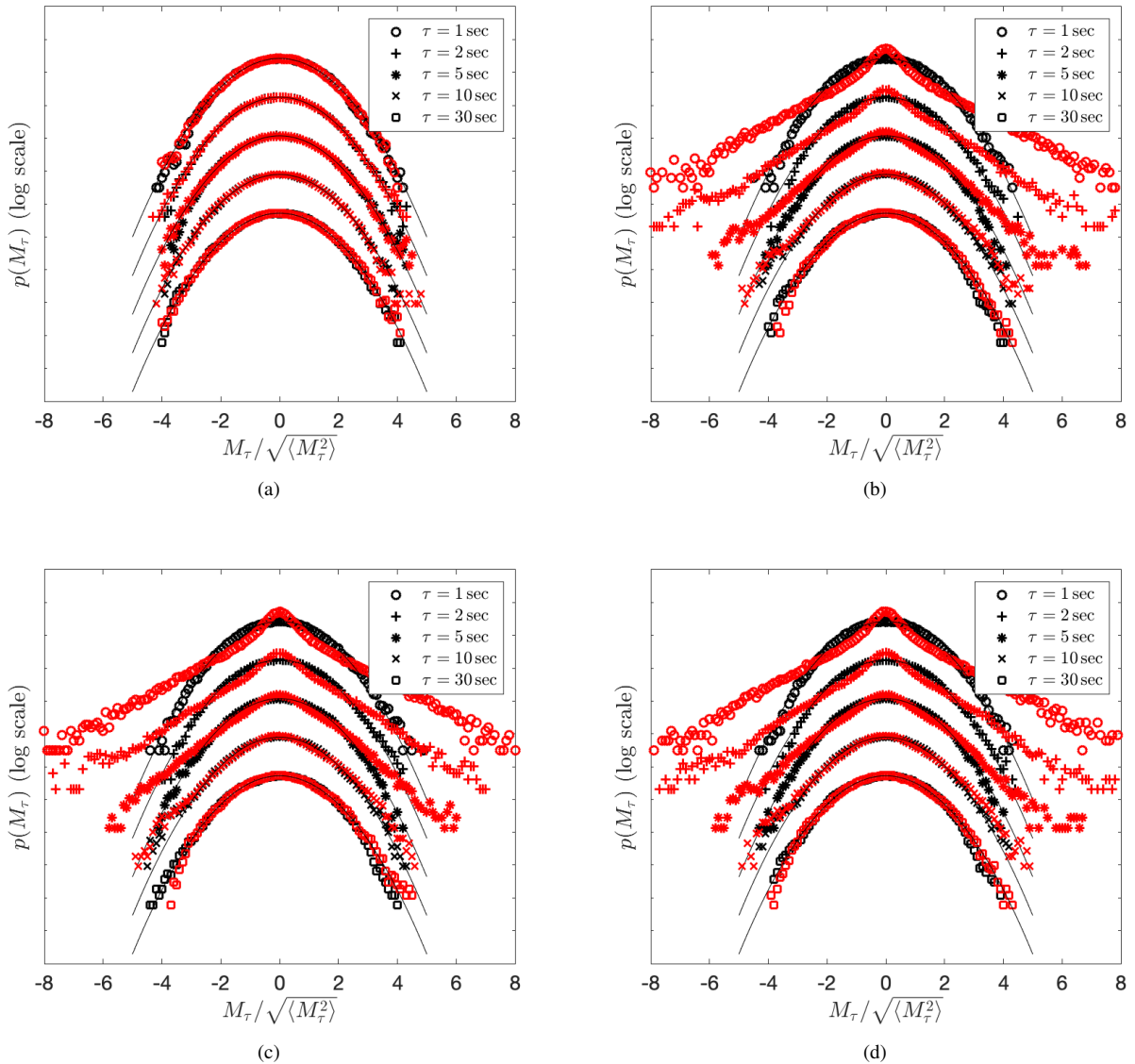
Figure 10. PDFs of load increments M_τ for (a) blade root flapwise bending moment (`RootFlap`) (b) rotor thrust (`Thrust`) (c) rotor torque (`Torque`) (d) tower fore-aft bending moment (`TwrForeAft`) of the 1.5MW turbine with Mann and Time-mapped Mann inflow wind fields at different temporal increments τ. The red markers correspond to the Time-mapped Mann field cases while black markers present the results for the Mann field cases. The black thin lines are Gaussian distributions as reference. The curves are shifted vertically for visualization.

The resulting load increments M_τ, except for the `RootFlap`, follow the characteristics of the wind velocity increments shown in Fig. 8. Clearly, the PDFs of the Mann load increments are very well described by the Gaussian distribution. On the contrary, the PDFs of the load increments resulting from the Time-mapped Mann field deviate significantly from the

360   Gaussian distribution for a range of scales. The observed heavy tails shown by the Time-mapped PDFs reflect, as mentioned earlier, a higher probability of extreme load fluctuations than the probability of a Gaussian distribution. The special case of the `RootFlap` is to be investigated in future work.

A more detailed description of the evolution of the intermittency of M_τ with τ is presented in Fig. 11. Here, the results
365   of $\text{Kurt}(M_\tau)$ from Eq. (11) are calculated exemplarily for the `Thrust` signal. It is clearly visible that the values of the kurtosis for the load case with the Time-mapped Mann wind field are higher than three (value of three indicates a Gaussian distribution) for all the values of τ up to around 20 seconds. This proves the intermittent characteristics of the loading. In contrast, the corresponding values for the Mann case fluctuate around three for all the considered time scales, agreeing with the Gaussian statistics. Additionally, for time scales below one sec, a decreasing intermittent behavior of the load is visible
370   in the Time-mapped case when decreasing τ. This might be directly related to the wind turbine and is subject to future research.

Further investigations should be done to explain the potential sources of the observable bumps in the kurtosis of the Time-mapped Mann case. A strong dependence of the peaks on the rotational frequency of the rotor has been recognized by the authors. However, the aim of this first turbine study was to investigate whether the intermittency which was introduced to the
375   wind field by deriving the Time-mapped Mann field carries over to turbine loads in general. This has clearly been shown here.
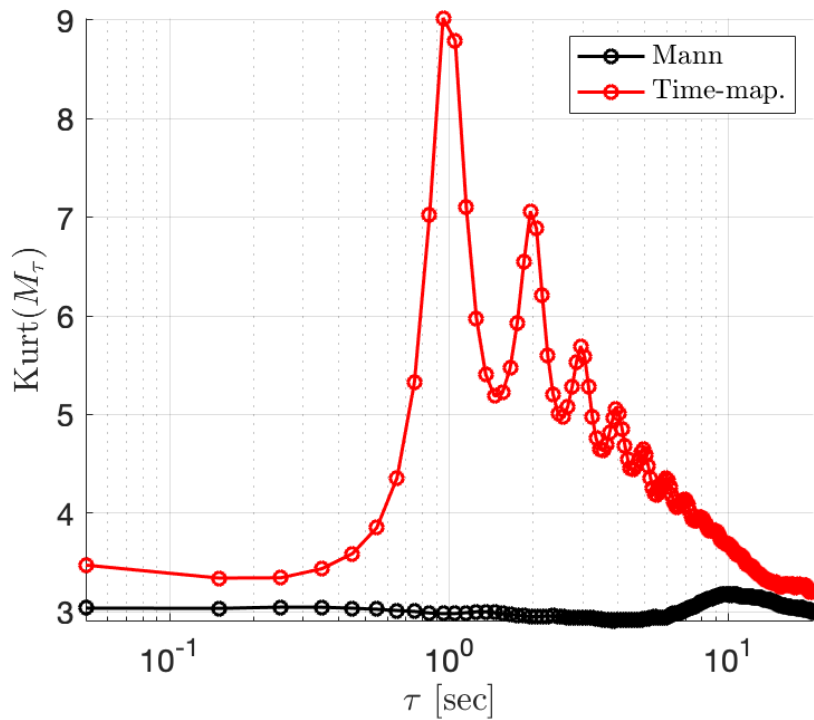
Figure 11. Kurtosis of the PDF of M_τ calculated for the `Thrust` according to Eq. (11) at different temporal increments τ. The red markers correspond to the Time-mapped Mann field while black markers present the results for the Mann field. A value of three corresponds to a Gaussian distribution.

5 Conclusions

In this work, a new synthetic wind field model has been introduced which combines spatial correlations from the well-known Mann model and the effect of intermittency. During the derivation, the time-mapping procedure from the so-called CTRW model has been applied to a Mann wind field in order to generate intermittency. This new model is called Time-mapped Mann

380 model. The CTRW model relies on stochastic differential equations for the velocity and assumes exponentially decaying velocity correlations. On the other hand, the Mann model is based on a proper modeling of the spectrum according to atmospheric conditions which is also recommended by the standard IEC 61400-1. With our procedure, we obtain a model which aims at keeping the spatial correlations in the transverse directions from the Mann model, and thus, following the IEC 61400-1 standard in this respect, and on the other hand adding intermittency which has also been reported as a feature inherent in wind

385 (Mücke et al. (2011)).

A comparison between Mann and the corresponding Time-mapped Mann fields was shown in detail in this work. The analysis of the velocity spectra, as well as the PDF and kurtosis of velocity increments showed that this method managed to generate

an intermittent wind field in the longitudinal direction. On the other hand, this method keeps the spatial correlation almost exactly as in the Mann field in the other two directions. This is due to the way the time mapping is applied where the velocity

390   field "slices" (x_2-x_3 planes) of the Mann field are shifted by random time shifts. Small differences in the compared statistics in transverse directions are due to the interpolation between the generated time shifted slices and the new, uniformly separated velocity field slices.

Furthermore, a first analysis and comparison of loads with respect to intermittency between Mann and Time-mapped wind fields on a 1.5MW wind turbine was done. The analysis of the loads showed that the intermittency is transported from the wind

395   field to the structure of the wind turbine. However, these loads are different in their response to the wind field intermittency. The increment statistics showed that in the analyzed case, rotor thrust, rotor torque, and tower fore-aft bending moment are strongly affected by the intermittency in the wind field, whereas the blade root bending moment shows less intermittency. The resulting non-Gaussian load increment distributions suggest that simulating wind turbines under Gaussian wind fields such as Mann wind fields could potentially lead to an underestimation of the probability of extreme loads.

400   An important future extension of the Time-mapped Mann model would be an incorporation of shear in the Mann model. This poses a challenge to the Time-mapping process since the slices could potentially not be simply shifted as it is done now. Future research in the investigation of the loads involves a deeper analysis of the effect of intermittency on the turbine loads, especially with respect to the effect of the rotational frequency of the rotor.

Appendix A: Analysis of a cubic field

405   For a further investigation of the effect of the time mapping of wind fields on the spectra, a Mann box with $n_{x_1} = n_{x_2} = n_{x_3} = 512$ and $\Delta x_1 = \Delta x_2 = \Delta x_3 = 1$ is studied in this appendix. The same comparison of spectra as described in Sec. 4.1 is studied here for this cubic field. In Fig. A1 (a), (b), and (c) it can be seen that the spectra show in general good agreement between the Mann and the Time-mapped Mann field. The spectra in the longitudinal direction x_1 in A1(a) show a discrepancy due to the time-mapping procedure which is applied to this direction. Further, all plots show increasing discrepancies for larger

410   wavenumbers which should be resulting from the interpolation procedure. Note that in Fig. 6(b) and (c) where the resolution in x_2- and x_3-direction was much coarser, the deviations already start at smaller wavenumbers. The comparison of coherence of the same two fields in Fig. A2 shows good agreement between the two fields in the x_2- and x_3-directions. The small deviations result from the interpolation routine.
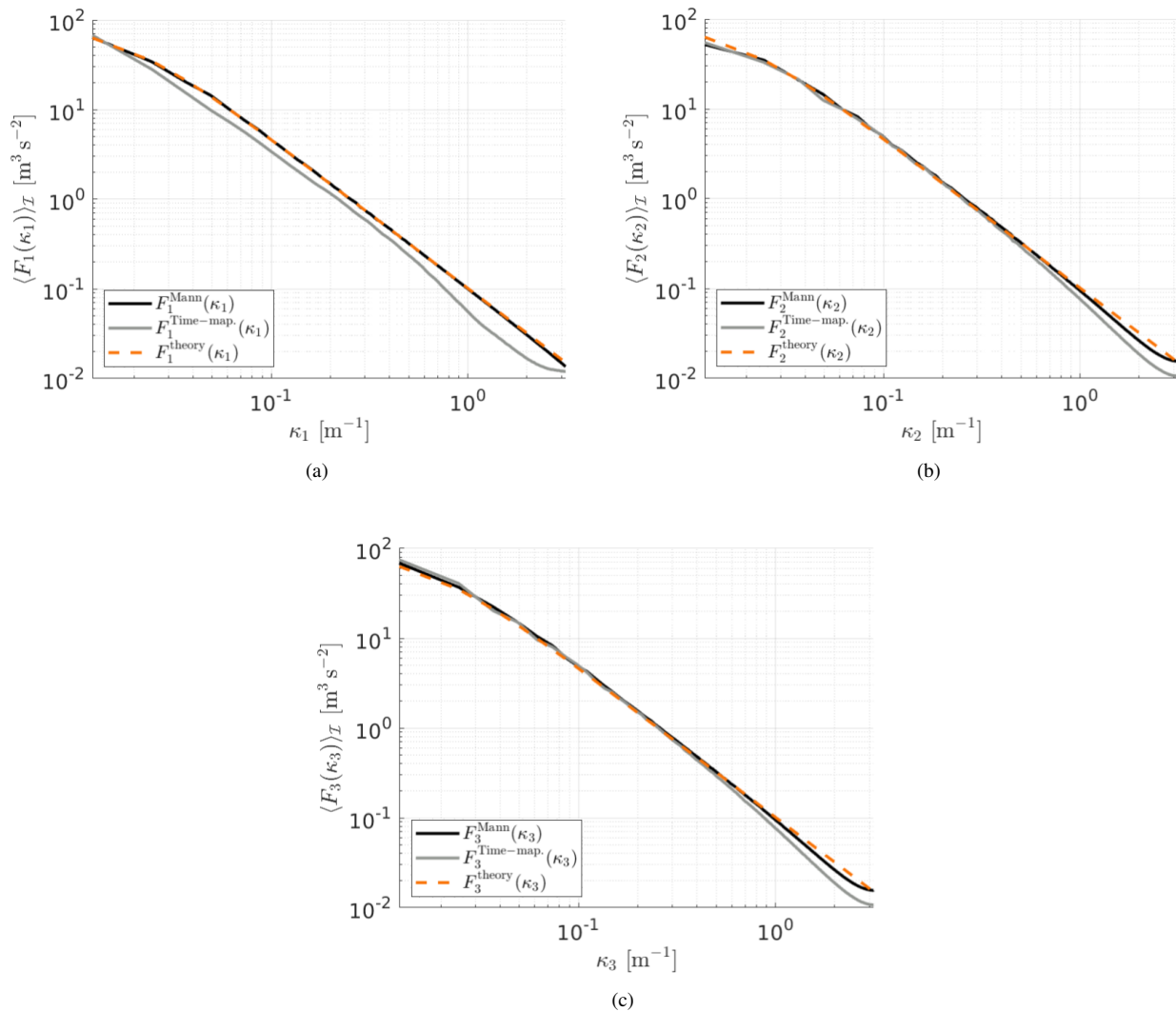
Figure A1. Comparison of averaged spectra in (a) x_1-, (b) x_2-, and (c) x_3-directions respectively for the Mann field, the Time-mapped field and the theoretical results calculated from Eq. (14)
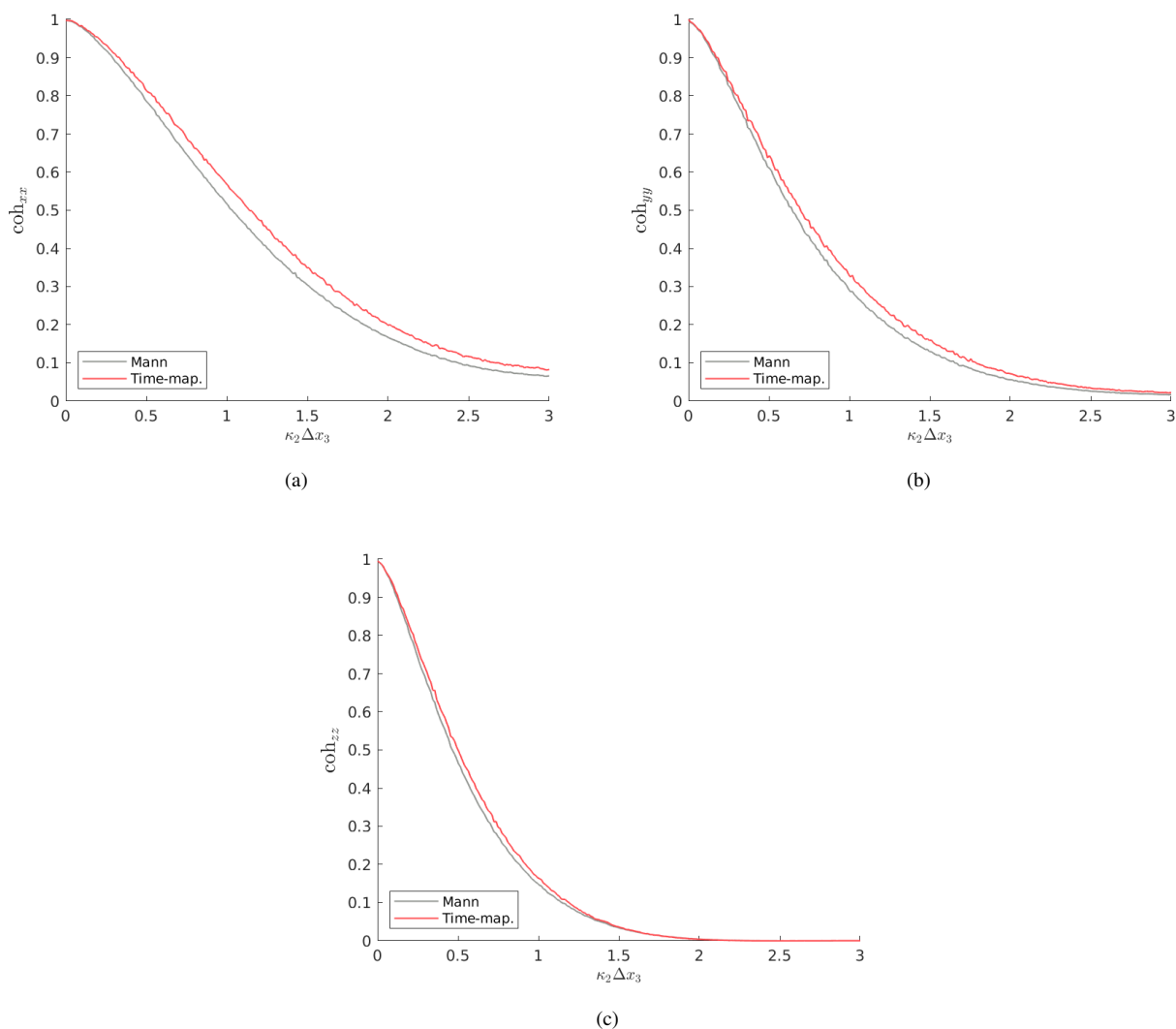
Figure A2. Comparison of the coherence of velocity components in (a) x_1-, (b) x_2-, and (c) x_3-directions for the Mann field and the Time-mapped Mann field over wavenumber $\kappa_2\Delta x_3$ with $\Delta x_3 = 2.6$ and $\Delta x_1 = 0$.

Author contributions.

415   KY performed the wind field simulations and the wind field analyses and wrote the paper (with contributions from the other authors). Preliminary evaluations were performed in the scope of the Master Thesis of AH at the Carl von Ossietzky University Oldenburg supervised by LJL and LH. All authors contributed to the generation of the method. DM performed the BEM simulations and the load analysis. HK and LH provided intensive reviews on the generation of the codes and the analyses. LJL

initiated the research, provided extensive consultation on the development of the method and the scientific analyses, and had a
supervising function.

Competing interests. The authors declare no conflict of interest.

Acknowledgements. The authors would like to acknowledge Mr. Jörg Schwarte, Nordex Energy SE & Co.KG for providing measured wind data. Parts of this work have been performed in the scope of the project EMUwind (03EE2031A/C), PASTA (03EE2024A/B), and SFB1463 (434502799). The EMUwind and PASTA projects are funded by the German Federal Ministry for Economic Affairs and Energy (Bundesministeriums für Wirtschaft und Energie-BMWi) due to a decision of the German Bundestag and the SFB1463 is funded by the German Research Foundation (Deutsche Forschungsgemeinschaft, DFG).

References

Berg, J., Natarajan, A., Mann, J., and Patton, E. G.: Gaussian vs non-Gaussian turbulence: impact on wind turbine loads, Wind Energy, 19,
430   1975–1989, 2016.

Boettcher, F., Renner, C., Waldl, H.-P., and Peinke, J.: On the statistics of wind gusts, Boundary-Layer Meteorology, 108, 163–173, 2003.

Böttcher, F., Barth, S., and Peinke, J.: Small and large scale fluctuations in atmospheric wind speeds, Stochastic Environmental Research and
       Risk Assessment, 21, 299–308, 2007.

Cuxart, J., Yagüe, C., Morales, G., Terradellas, E., Orbe, J., Calvo, J., Fernández, A., Soler, M., Infante, C., Buenestado, P., Espinalt, A.,
435   Joergensen, HE andRees, J., Vilá, J., Redondo, J., Cantalapiedra, I., and Conangla, L.: Stable atmospheric boundary-layer experiment in
       Spain (SABLES 98): a report, Boundary-layer meteorology, 96, 337–370, 2000.

ESDU: Characteristics of wind speed in the lower layers of the atmosphere near the ground: Strong winds (neutral atmosphere), The Unit,
       1982.

Fogedby, H. C.: Langevin equations for continuous time Lévy flights, Physical Review E, 50, 1657, 1994.

440 Friedrich, J., Peinke, J., Pumir, A., and Grauer, R.: Explicit construction of joint multipoint statistics in complex systems, Journal of Physics:
       Complexity, 2021.

Gioffre, M., Gusella, V., and Grigoriu, M.: Simulation of non-Gaussian field applied to wind pressure fluctuations, Probabilistic Engineering
       Mechanics, 15, 339–345, 2000.

Gong, K. and Chen, X.: Influence of non-Gaussian wind characteristics on wind turbine extreme response, Engineering structures, 59, 727–
445   744, 2014.

Gontier, H., Schaffarczyk, A., Kleinhans, D., and Friedrich, R.: A comparison of fatigue loads of wind turbine resulting from a non-Gaussian
       turbulence model vs. standard ones, in: Journal of physics: conference series, vol. 75, p. 012070, IOP Publishing, 2007.

GWEC: GWEC Global Wind Energy Report 2021, Global Wind Energy Council, 2021.

Han, C.-H.: International Electrotechnical Commission, Electric Engineers Magazine, pp. 29–34, 2007.

450 Jonkman, B. and Jonkman, J.: NWTC Design Code FAST v6.01., Tech. rep., National Renewable Energy Laboratory, 2005.

Jonkman, B. and Jonkman, J.: NWTC Design Code FAST v8.16.00a-bjj, Tech. rep., National Renewable Energy Laboratory, 2016.

Kaimal, J. C., Wyngaard, J., Izumi, Y., and Coté, O.: Spectral characteristics of surface-layer turbulence, Quarterly Journal of the Royal
       Meteorological Society, 98, 563–589, 1972.

Kelly, M.: From standard wind measurements to spectral characterization: turbulence length scale and distribution, Wind Energy Science, 3,
455   533–543, 2018.

Kleinhans, D.: Stochastische Modellierung komplexer Systeme—Von den theoretischen Grundlagen zur Simulation atmosphärischer Wind-
       felder, Ph.D. thesis, Westfälischen Wilhelms-Universität Münster, 2008.

Kleinhans, D. and Friedrich, R.: Continuous-time random walks: Simulation of continuous trajectories, Physical Review E, 76, 061 102,
       2007.

460 Körber, F., Besel, G., and Reinhold, H.: Messprogramm an der 3 MW Windkraftanlage GROWIAN: Förderkennzeichen: 03E-4512-A, Tech.
       rep., 1988.

Larsen, T. J. and Hansen, A. M.: How 2 HAWC2, the user's manual, 2007.

Liu, L., Hu, F., Cheng, X.-L., and Song, L.-L.: Probability density functions of velocity increments in the atmospheric boundary layer,
       Boundary-layer meteorology, 134, 243–255, 2010.

465   Malcolm, D. and Hansen, A.: WindPACT Turbine Rotor Design Study: June 2000–June 2002 (Revised), Tech. rep., National Renewable Energy Lab.(NREL), Golden, CO (United States), 2006.

Mann, J.: The spatial structure of neutral atmospheric surface-layer turbulence, Journal of fluid mechanics, 273, 141–168, 1994.

Mann, J.: Wind field simulation, Probabilistic engineering mechanics, 13, 269–282, 1998.

MATLAB: version 9.7.0.1586710 (R2019b), Natick, Massachusetts, 2019.

470   Morales, A., Wächter, M., and Peinke, J.: Characterization of wind turbulence by higher-order statistics, Wind Energy, 15, 391–406, 2012.

Mücke, T., Kleinhans, D., and Peinke, J.: Atmospheric turbulence and its influence on the alternating loads on wind turbines, Wind Energy, 14, 301–316, 2011.

Pope, S. B.: Turbulent flows, IOP Publishing, 2001.

Schlichting, H. and Gersten, K.: Boundary-layer theory, Springer, 2016.

475   Schottler, J., Reinke, N., Hölling, A., Whale, J., Peinke, J., and Hölling, M.: On the impact of non-Gaussian wind statistics on wind turbines– an experimental approach, Wind Energy Science, 2, 1–13, 2017.

Schwarz, C. M.: Wind turbine load dynamics in the context of intermittent atmospheric turbulence, Ph.D. thesis, Carl von Ossietzky Universität Oldenburg, 2020.

Schwarz, C. M., Ehrich, S., Martín, R., and Peinke, J.: Fatigue load estimations of intermittent wind dynamics based on a Blade Element

480   Momentum method, in: Journal of Physics: Conference Series, vol. 1037, p. 072040, IOP Publishing, 2018.

Schwarz, C. M., Ehrich, S., and Peinke, J.: Wind turbine load dynamics in the context of turbulence intermittency, Wind Energy Science, 4, 581–594, 2019.

Taylor, G. I.: The spectrum of turbulence, Proceedings of the Royal Society of London. Series A-Mathematical and Physical Sciences, 164, 476–490, 1938.

485   Uhlenbeck, G. E. and Ornstein, L. S.: On the theory of the Brownian motion, Physical review, 36, 823, 1930.

Vindel, J., Yagüe, C., and Redondo, J.: Structure function analysis and intermittency in the atmospheric boundary layer, Nonlinear Processes in Geophysics, 15, 915–929, 2008.

von Kármán, T.: Progress in the statistical theory of turbulence, Proceedings of the National Academy of Sciences of the United States of America, 34, 530, 1948.

490   Weron, R.: Levy-stable distributions revisited: tail index> 2 does not exclude the Levy-stable regime, International Journal of Modern Physics C, 12, 209–223, 2001.